Geophysical Journal International

Geophys. J. Int. (2018) **215,** 585–599
Advance Access publication 2018 July 20
GJI Seismology

doi: 10.1093/gji/ggy298

Statistical characteristics of scattered waves in three-dimensional random media: comparison of the finite difference simulation and statistical methods

Kentaro Emoto and Haruo Sato

Geophysics, Graduate School of Science, Tohoku University, Sendai, Japan. E-mail: kentaro.emoto@tohoku.ac.jp

Accepted 2018 July 19. Received 2018 July 12; in original form 2018 January 3

SUMMARY

Random velocity fluctuations distributed in the solid Earth function as sources of seismic wave scattering. Scattering effects are often observed in high-frequency seismograms of earthquakes as the broadening of the apparent duration of an *S*-wavelet and the emergence of coda waves. We conduct large-scale 3-D finite difference (FD) simulations of the scalar wave equation to analyse the intensities of scattered waves propagating through random small-scale heterogeneous media. First, we compare ensemble averaged intensities (mean square amplitudes) derived by the FD simulation with those synthesized based on statistical methods such as the radiative transfer equation with the Born approximation and the newly developed spectrum division methods. We consider several types of random media characterized by von Kármán type autocorrelation functions with different characteristic distances and mean square fractional fluctuations. In the case of a large characteristic distance, the forward scattering is dominant and the fluctuation of the traveltime is large. Even in that case, the newly developed spectrum division method can reproduce the average intensity derived by FD simulations in the entire lapse time range. We further investigate the characteristics of scattered waves. To know the property of the fluctuation of intensities due to the small-scale heterogeneity is important for the ground motion prediction. We reveal the gradual shift of intensity fluctuations from the log-normal distribution to the exponential one with the increase of lapse time. The timing of the shift varies depending on the random medium parameters. This can be explained as the shift from the multiple forward scattering regime to the incoherent wide-angle scattering one. The decay rate of the intensity changes from r^{-2} to r^{-4} with the increase of the propagation distance r, which corresponds to the empirical relationship of the observed intensity. This timing of the change also depends on the random medium parameters.

Key words: Numerical modelling; Wave propagation; Wave scattering and diffraction.

1 INTRODUCTION

Coda waves have been analysed as scattered waves by random small-scale heterogeneities distributed in the solid Earth since the pioneering work of Aki & Chouet (1975). Coda waves are thought as incoherent scattered waves and the spatial distribution of their intensity at a late lapse time becomes almost uniform and isotropic. Those characteristics have been used as the bases of coda analyses. We show an observational example of the spatial distribution of the energy in Fig. 1. The coda energy level decreases as lapse time increases and its distribution becomes nearly flat around the epicentre at a large lapse time.

The other characteristic of the coda is that it consists of scattered waves with random phases. Takahara & Yomogida (1992) showed that the root mean square (RMS) envelope of the coda obeys the Rayleigh distribution. Nakahara & Carcole (2010) considered the Nakagami distribution to model the amplitude fluctuation of coda and they found that it could be modelled by the Rayleigh distribution as a special case of the Nakagami distribution. This characteristic can be explained by considering coda as a Gaussian noise which has random phases. When the amplitude obeys the Rayleigh distribution, the intensity obeys the exponential distribution. Conversely, intensities just after the direct arrival obey the log-normal distribution (Rytov *et al.* 1989; Yoshimoto *et al.* 2015). This can be explained as the result of multiple forward scattering. When the amplitude obeys the log-normal distribution, the squared amplitude also obeys the log-normal distribution. Therefore, the fluctuations of the intensity shift from the log-normal distribution to the exponential one. The timing and the medium parameter dependence have not been investigated yet. To know the property of the fluctuation is important to deepen the understanding of the basics of scattered wavefields. This is also important for the prediction of

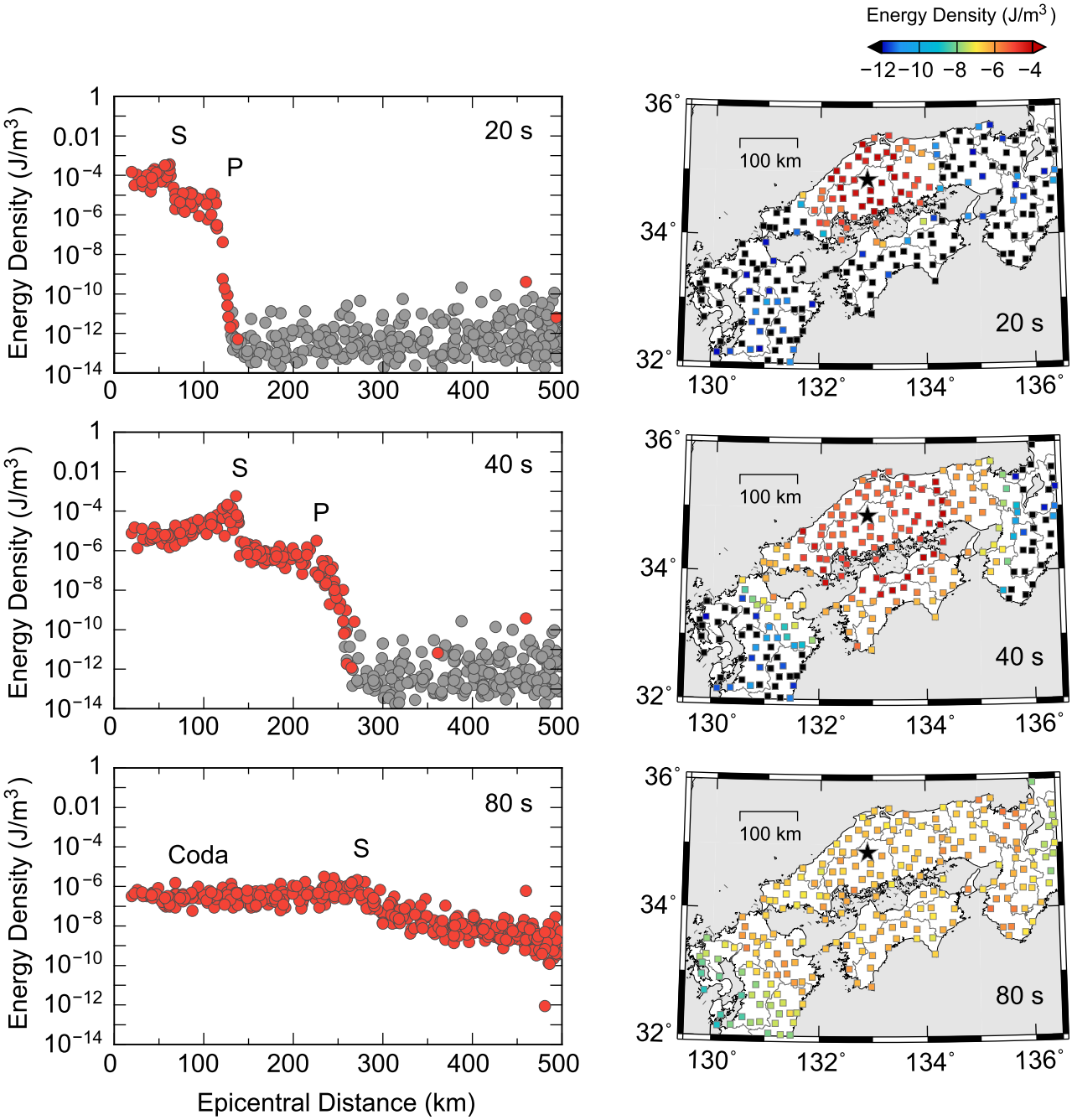

Figure 1. The left panel shows snapshots of observed energy density at the frequency band of 2–4 Hz at lapse times of 20, 40 and 80 s. Red and grey circles represent that the signal to noise ratio is higher and lower than 5, respectively. The right panel shows the epicentre of the earthquake (date: 2011 November 21, magnitude: 5.2, depth: 12 km) by a black star and Hi-net stations (Okada *et al*. 2004; Obara *et al*. 2005) by squares. The energy density is calculated as the sum of squared velocity seismograms of three components.

the strong ground motion to estimate the possible error range due to the small-scale heterogeneity. The amplitudes of observed seismograms are affected not only by the small-scale heterogeneity but also by other factors, such as the site amplification factor, the source size, the radiation pattern of the source and the intrinsic attenuation. Therefore, to investigate the effect of the small-scale heterogeneity on the amplitude fluctuation, the role of the numerical simulation is important.

In order to investigate the characteristics of wave propagation in random small-scale heterogeneous media, there have been developments of theoretical approaches to describe the averaged intensity of waves. In the theoretical approach, an ensemble of random media is considered. Random media are statistically characterized by the autocorrelation function (ACF) of random velocity fluctuation, which is parametrized by a characteristic distance (a), an RMS fractional velocity fluctuation (ϵ) and a roll-off parameter of the spectrum

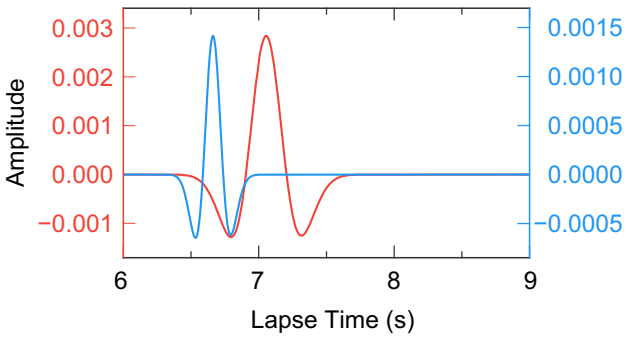

Figure 2. Ricker wavelets at $r = 25$ km for $f_c = 1.5$ Hz (red) and $f_c = 3.0$ Hz in a homogeneous medium with $V_0 = 4$ km s^{-1}. Left and right axes indicate the amplitude for $f_c = 1.5$ Hz and $f_c = 3.0$ Hz, respectively.

decay (κ) at large wavenumbers. Following theoretical methods have been widely known: the radiative transfer equation (RTE) with the Born approximation (e.g. Chandrasekhar 1960; Chernov 1960; Margerin 2005), the diffusion approximation (e.g. Ishimaru 1978) and the Markov approximation based on the parabolic approximation, which is a stochastic extension of the phase screen method (e.g. Shishov 1974; Rytov *et al.* 1989; Sato 1989). We note that those methods have been applied to observed data. For example, Przybilla *et al.* (2009) and Silva *et al.* (2018) stacked observed seismograms to obtain the averaged envelopes and estimated the intrinsic and the scattering attenuations by applying the RTE for elastic waves. Because each approximation has both advantages and disadvantages, we need to properly choose a method depending on the purpose and the situation. Also, it is necessary to validate the approximation by comparing with the numerical simulation.

Recently, Sato (2016, referred to as Paper I in the following) proposed a new method to solve the intensity propagation through von Kármán type random media. Dividing the power spectrum density function (PSDF) of random media into short- and long-scale components, Paper I applies the Markov approximation for the long-scale components and estimated the scattering loss by applying the Born approximation to the short-scale component. This method analytically solves the intensity, especially around the peak arrival. We refer to this method as the spectrum division method I in the following. However, this method is not able to synthesize the intensity in the late coda. By extending the method proposed by Paper I, Sato & Emoto (2017, referred to as Paper II in the following) have developed a new method to solve especially when $ak_c \gg 1$ and $\varepsilon^2 a^2 k_c^2 \gtrsim O(1)$. They apply the Markov approximation and the RTE with the Born approximation for the long- and the short-scale components, respectively. It is a new idea that they convolved the intensity calculated by the RTE for the short-scale component with the broadening effects as scattering contribution of the long-scale component in the time domain (hereafter referred to as the spectrum division method II).

To verify the reliability of proposed theoretical methods, we need to compare synthesized intensities by those methods with numerical simulations of the wave propagation in random heterogeneous media. Numerical simulations of the wave propagation in random small-scale heterogeneous media have been conducted since the 1980s (e.g. Frankel & Clayton 1986; Jannaud *et al.* 1991; Ikelle *et al.* 1993; Shapiro & Keib 1993). Recently, the numerical simulation of the wave propagation in 3-D random media has been conducted to analyse the effect of the scattering on the ground motion (Imperatori & Mai 2013) and the sensitivity of the medium change (Obermann *et al.* 2016). However, the computational costs of the 3-D numerical simulation are high. Especially, the simulation of coda waves requires a large model space because any boundary condition affects the coda waves. So the validity of the theoretical methods in 2-D random media has been often analysed. In 2-D random media, the comparison of intensities derived by the Markov approximation with the finite difference (FD) simulation of the wave equation has been conducted (e.g. Fehler *et al.* 2000; Saito *et al.* 2003; Korn & Sato 2005; Emoto *et al.* 2012). Sato & Fehler (2016) successfully showed a good fit of the spectrum division method I and FD simulations for von Kármán type random media except for the coda part. In the 3-D random media, Przybilla & Korn (2008) compared the FD simulation with the Markov approximation and the RTE at short propagation distances. They concluded that the RTE can be used to model the intensity even when $ak_c \gg 1$ by convolving the wandering term which means statistical fluctuation of traveltimes. We note that Paper II also successfully showed a good fit of averaged intensities of the spectrum division method II and FD simulations for a large size of random media, where the model space is a long and narrow rectangular parallelepiped for the study of intensity variation with travel distance increases. However, the comparison of late coda has not been conducted yet.

In this paper, we conduct FD simulations of scalar waves in 3-D random media of exponential type ACFs ($\kappa = 0.5$). First, we compare averaged intensities derived by the FD simulation and those synthesized by using the proposed theoretical methods to check their validities. Different from Paper II, the model space is a large cube for the study of coda intensity variation with the increase of lapse time. In addition to these data, we reanalyse the same data as used in Paper II. Next, we investigate the characteristics of intensities of scattered waves, such as the lapse time dependence of the distribution of intensities and the attenuation rate per travel distance due to the small-scale heterogeneities.

2 METHOD

2.1 Wave equation in random media

The scalar wave u is governed by the wave equation in a 3-D inhomogeneous medium:

$$\nabla^2 u(\boldsymbol{x}, t) - \frac{1}{V(\boldsymbol{x})^2}\ddot{u}(\boldsymbol{x}, t) = f(\boldsymbol{x}, t), \tag{1}$$

where $\boldsymbol{x} = (x, y, z)$ and f is the source term. We consider that the medium velocity is fluctuated as $V(\boldsymbol{x}) = V_0(1 + \xi(\boldsymbol{x}))$, ξ is a random variable. Here, we imagine an ensemble of the random fluctuation $\{\xi\}$ with ξ=0, where $\langle\,\rangle$ denotes the ensemble average. We assume that the fluctuation is weak, $\epsilon^2 \equiv \xi^2 \ll 1$. The ensemble averaged velocity $V_0 = \langle V(\boldsymbol{x})\rangle$ is chosen to be 4 km s^{-1}. When the random fluctuation is a von Kármán type, the PSDF is written as

$$P_{\mathrm{vK}}(m) = \frac{8\pi^{\frac{3}{2}}\Gamma\left(\kappa + \frac{3}{2}\right)\varepsilon^2 a^3}{\Gamma(\kappa)(1 + a^2m^2)^{\kappa+\frac{3}{2}}}, \tag{2}$$

where m is the wavenumber of the fluctuation.

We put a special focus on von Kármán type random media with $\kappa = 0.5$, which is an exponential type. The ACF and the PSDF are written as

$$R_{\mathrm{exp}}(r) = \varepsilon^2 \mathrm{e}^{-\frac{r}{a}}, \tag{3a}$$

and

$$P_{\mathrm{exp}}(m) = \frac{8\pi\varepsilon^2 a^3}{(1 + a^2m^2)^2}. \tag{3b}$$

Table 1. List of statistical medium parameters. In all cases, $V_0 = 4\,\mathrm{km\ s^{-1}}$. t_T is the transport mean free time, which is calculated from P. Cases 5–7 are the same as analysed in Paper II.

Case	f_c (Hz)	k_c ($\mathrm{km^{-1}}$)	a (km)	ϵ	κ	ak_c	$\epsilon^2 a^2 {k_\mathrm{c}}^2$	t_T (s)	Description
1	1.5	2.4	1	0.05	0.5	2.4	1.39×10^{-2}	45.7	Weak forward scattering
2	1.5	2.4	5	0.01	0.5	12	1.39×10^{-2}	2.35×10^{3}	Forward but weak scattering
3	1.5	2.4	5	0.05	0.5	12	3.47×10^{-1}	93.9	Forward scattering
4	1.5	2.4	10	0.05	0.5	24	1.39	149	Strong forward scattering
5	3.0	4.7	5	0.05	0.1	24	1.39	59.6	Rich small-scale component
6	3.0	4.7	5	0.05	0.5	24	1.39	74.6	–
7	3.0	4.7	5	0.05	1.0	24	1.39	164	Poor small-scale component

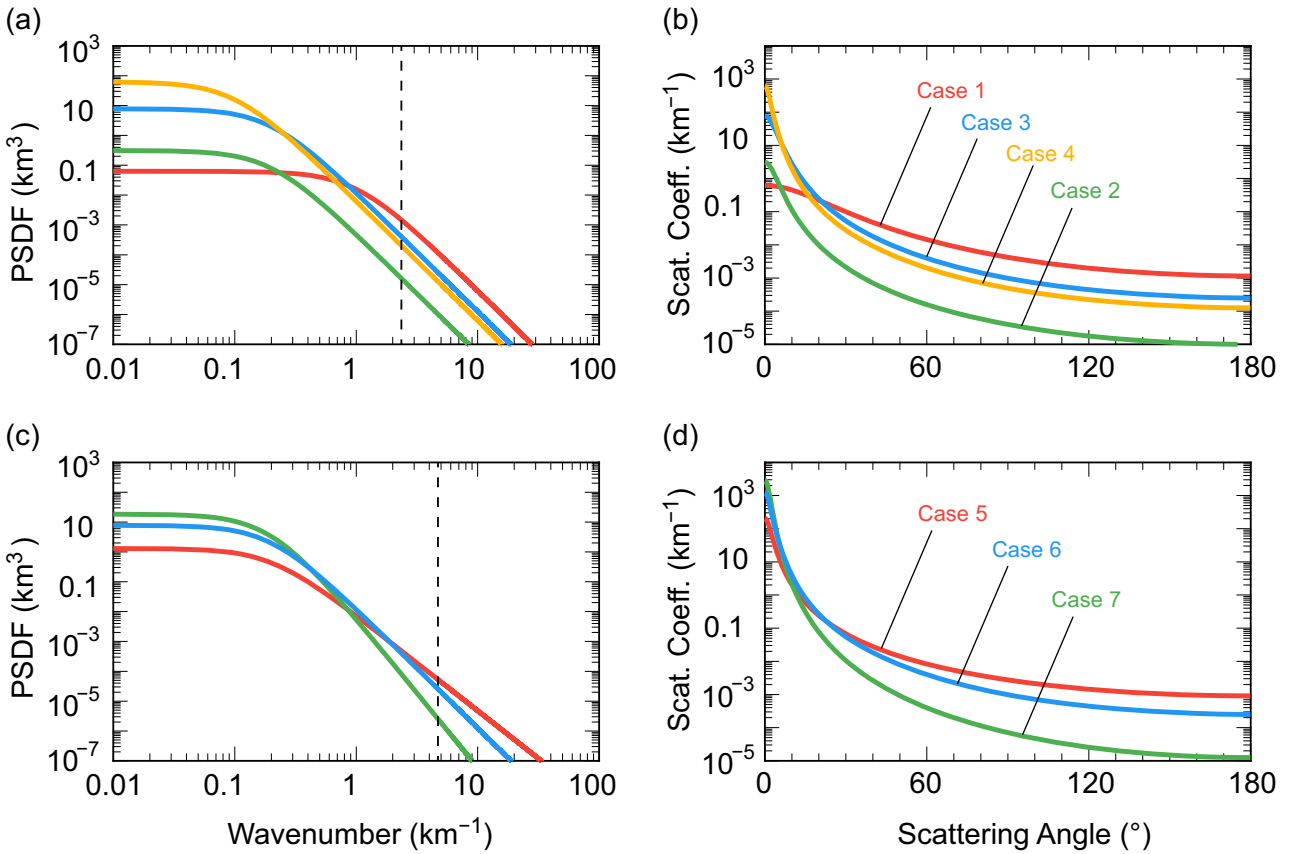

Figure 3. (a) PSDFs and (b) scattering coefficients $g^B(k_\mathrm{c}, \psi)$ by the Born approximation for cases 1–4. Red, green, blue and yellow colours indicate cases 1–4, respectively. (c) and (d) are the same as (a) and (b) but for cases 5–7. Red, blue and green colours indicate cases 5–7, respectively. The vertical dashed lines in (a) and (c) indicate k_c=2.4 $\mathrm{km^{-1}}$ for 1.5 Hz and k_c=4.7 $\mathrm{km^{-1}}$ for 3.0 Hz, respectively.

We focus on the propagation of a Ricker wavelet with the central frequencies f_c=1.5 and 3.0 Hz, whose centre-wavenumbers are k_c = 2.4 $\mathrm{km^{-1}}$ and 4.7 $\mathrm{km^{-1}}$, respectively (see Fig. 2). We consider four cases of random medium parameters for $f_\mathrm{c} = 1.5$ Hz and three cases for $f_\mathrm{c} = 3.0$ Hz as enumerated in Table 1. The latter three cases are the same as those studied in Paper II. The PSDFs for all the cases are shown in Figs 3(a) and (c). Cases 2 and 3 have the same corner wavenumber at a^{-1}=0.2 $\mathrm{km^{-1}}$, but the DC levels are different. For case 1, the corner wavenumber is larger than other cases, but the DC level is the smallest. The case 4 has the smallest corner wavenumber. Cases 5–7 have the same corner wavenumber but different roll-off at high wavenumber range. For case 5, the DC level of the PSDF is small, but it has rich high-wavenumber components. Conversely, the high-wavenumber components are small for case 7. For case 6, the PSDF is the same as case 3, but the centre-wavenumber is 4.7 $\mathrm{km^{-1}}$. In cases 5 and 7, we put $\kappa = 0.1$ and 1.0, respectively.

The scattering power per unit volume is characterized by the scattering coefficient. In Figs 3(b) and (d), we show the angular dependence of the scattering coefficient according to the Born approximation,

$$g^B(k_\mathrm{c}, \psi) = \frac{k_\mathrm{c}^4}{\pi} P(2k_\mathrm{c} \sin\frac{\psi}{2}) \tag{4}$$

(see Paper II, eq. 9). For all the cases, scattering coefficients have a peak at 0°. It means that the forward scattering is dominant. The forward scattering becomes stronger with increasing ak_c. In case 1, forward scattering is relatively small and wide-angle scattering is relatively large compared to other cases. In the Born approximation, the condition of $\varepsilon^2 a^2 k_\mathrm{c}^2 \ll 1$ is required (see Paper II). This means that the phase shift during the scattering process should be small. For cases 4–7, $\varepsilon^2 a^2 k_\mathrm{c}^2$=1.39, so the Born approximation breaks down.

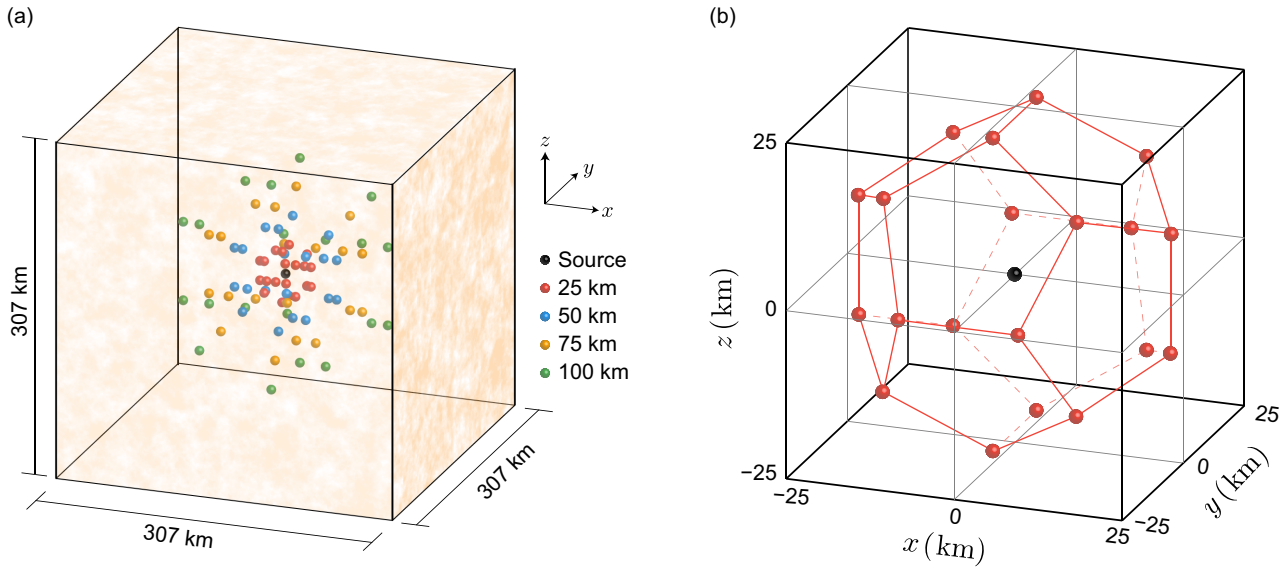

Figure 4. (a) Setting of a source and receivers in the model space for FD simulations for cases 1–4. Coloured spheres indicate receivers, where different colours indicate different distances from the source (black sphere). At each distance, receivers located at the vertices of a regular dodecahedron. (b) Magnified view of receivers at a propagation distance of 25 km.

2.2 Finite difference simulation

In practice, a random medium is realized (synthesized) by using the fast Fourier transform (FFT). The random variable $\xi(\boldsymbol{x})$ is the inverse Fourier transform of the square root of the PSDF multiplied by random phases. For large-scale computation, it is difficult to synthesize a random medium due to the physical memory limitation. To overcome this limitation, we merge small random media generated by using different seeds and create a large random medium. Each small medium overlaps with adjacent media. The overlap length is set to be the characteristic distance and the fluctuation is weighted by a cosine taper function. The details of making a large-scale random medium are described in Supporting Information Section S1. We use the FFTE package to perform the 3-D FFT, which supports the Message Passing Interface (MPI) parallel computation Takahashi (2010).

We numerically solve the scalar wave equation by using the FD method. The model space for cases from 1 to 4 is a cube of 307^3 km^3 (see Fig. 4). A source placed at the centre of the model space isotropically radiates a Ricker wavelet with f_c=1.5 Hz. The centre wavelength for the average velocity is 2.7 km. We smoothly remove the random fluctuation around the source by using a cosine taper function to avoid the fluctuation of the source radiation energy. We adopt the second- and fourth-order central difference schemes for time and space, respectively. The time step is 6 ms and the space interval is 80 m. The number of grid points is 3840^3. There are enough grid points per wavelength to avoid the effect of the grid dispersion. We set receivers at propagation distances of 25, 50, 75 and 100 km. Receivers are spherically distributed as vertices of a regular dodecahedron. Therefore, there are 20 receivers at each propagation distance. We assume that these receivers are statistically independent of each other. We conduct FD simulations for 18 realizations of random media, therefore there are 360 traces at each propagation distance as the elements of the ensemble. We show the example of traces in Supporting Information Section S2 and describe the convergence of the ensemble average in Supporting Information Section S3. We adopt the MPI parallel computation (e.g. Furumura & Chen 2004) and the computation is conducted on the Earth Simulator, a supercomputer managed by Japan Agency for Marine-Earth Science and Technology (JAMSTEC). It takes about 45 min for each simulation by using 128 nodes. We define the wave intensity of each wave time trace (hereafter called FD intensity) by using the Hilbert transform as

$$I(\boldsymbol{x}, t) = \frac{1}{2}\left\{u(\boldsymbol{x}, t)^2 + \mathcal{H}\left[u(\boldsymbol{x}, t)\right]^2\right\}, \tag{5}$$

where $\mathcal{H}$ indicates the Hilbert transform. The mean intensity, mean square (MS) amplitude, is calculated by averaging intensities of 360 traces (hereafter called averaged FD intensity).

The detail of the setting of the FD simulation for cases 5–7 is described in Paper II (see fig. 7), where the number of realizations of random media is 6 and there are nine receivers at each travel distance.

2.3 Monte Carlo simulation for the RTE with the Born scattering coefficient

We synthesize the intensity of a scalar wavelet by using the Monte Carlo simulation of the RTE, where the scattering coefficient is calculated by using the Born approximation (see eq. 4). The Monte Carlo simulation stochastically calculates the scattering of particles, where each particle carries a unit intensity (e.g. Gusev & Abubakirov 1987; Hoshiba 1991; Yoshimoto 2000; Przybilla & Korn 2008; Sens-Schönfelder *et al.* 2009). The scattering probability is calculated from the scattering coefficient. We isotropically shoot particles and calculate the propagation trajectory of each particle with a small time step. The time step is 0.01 s, which should be much smaller than the mean free time. The total propagation time is 70 s. At each time step, we count the number of particles in a spherical shell with a thickness of 1 km. Dividing the counted number by the volume of the spherical shell and the total number of particles, we obtain the intensity at a given travel distance, which is the intensity Green function, G_R. The total number of shot particles is 10^7 to stabilize intensity time traces. The calculation code is written in Java. It takes about 10–20 min for each calculation by using six threads of Intel Core i7-3770K. Convolution of G_R with

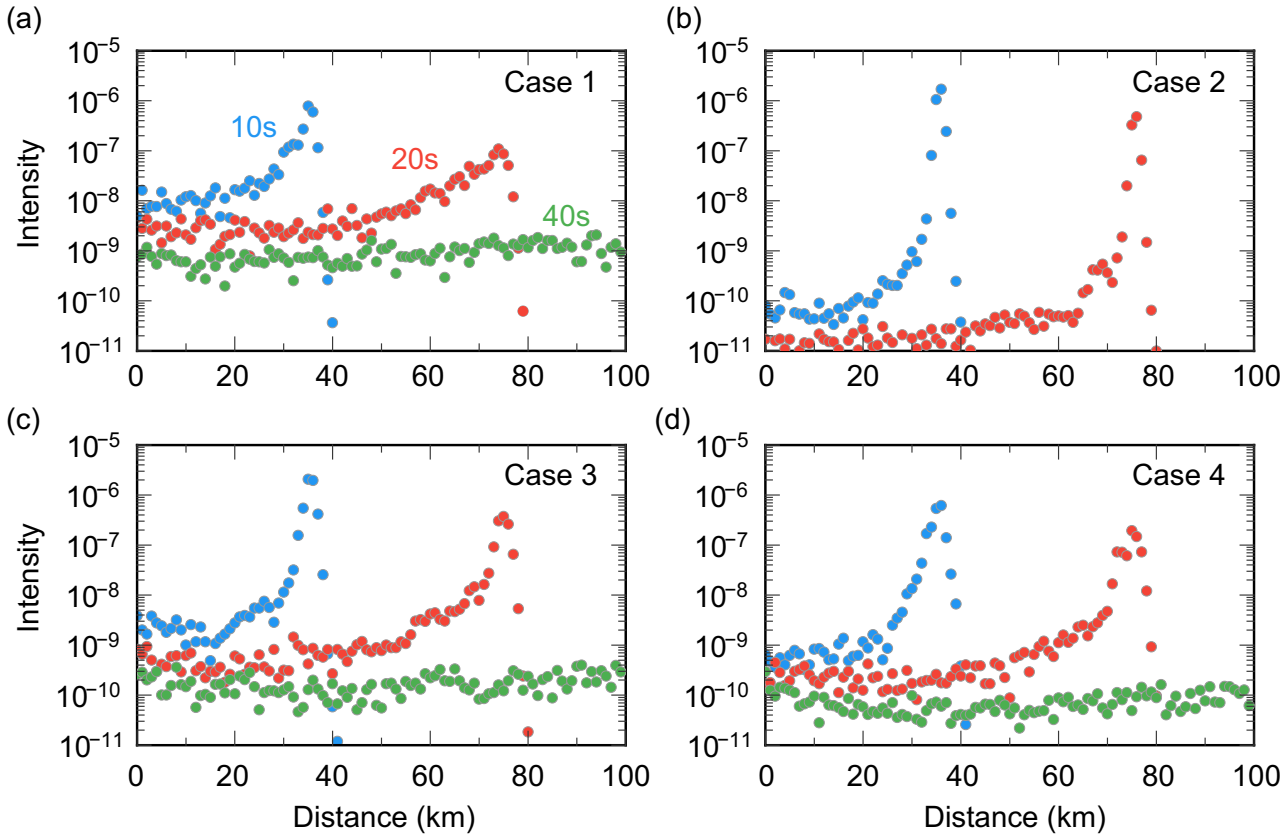

Figure 5. Snapshots of the spatial distribution of the intensity at lapse times of 10 s (blue), 20 s (red) and 40 s (green) for four cases. (a)–(d) correspond to cases 1–4, respectively. For case 2 (b), the intensity at 40 s is below the lower limit of the plot. We set 600 receivers on the x-, y-, and z-axes with an interval of 1 km and stack 6 traces to calculate the intensity at each distance.

the intensity of a Ricker source wavelet $s(t)$ gives the intensity time trace $I_R = G_R \otimes s$, where $\otimes$ denotes the convolution. In addition, we need to correct the traveltime fluctuation, when we compare the intensity derived by the RTE with that by the FD simulation as proposed by Przybilla & Korn (2008). The statistical contribution of traveltime fluctuations is called the wandering effect Lee & Jokipii (1975); Sato (2006); Sato & Emoto (2017). For the exponential type random media, the wandering term at a propagation distance r is

$$w(r,t) = \frac{1}{\sqrt{\pi}t_W(r)} e^{-\frac{t^2}{t_W(r)^2}}, \tag{6a}$$

where t_W is the characteristic time of the wandering effect, defined as

$$t_W(r) = \frac{2}{V_0}\sqrt{\varepsilon^2 a r}, \tag{6b}$$

(see Paper II, eqs 11 and 13). We note that $\int_{-\infty}^{\infty} w(r,t)\mathrm{d}t = 1$. Convolving the wandering term with the intensity derived by the Monte Carlo simulation, we can obtain the intensity involving the traveltime fluctuation as $I_{w,R} = I_R \otimes w$.

2.4 Spectrum division method I

When $ak_c \gg 1$, the forward scattering is dominant and the variation of the wave along the source-receiver path is slow. In this case, the Markov approximation based on the parabolic approximation can be used to calculate the intensity around the peak arrival (Sato *et al.* 2012,Chap. 9). In the Markov approximation, we need to solve the parabolic type wave equation for the two frequency mutual coherence function (TFMCF). The intensity time trace can be obtained by taking the inverse Fourier transform of the TFMCF at a given travel distance. Paper I proposed to divide the PSDF into two parts: long- and short-scale components. To define the PSDF of the short-scale component, we let the corner wavenumber as

$$a_S^{-1} = \zeta k_c, \tag{7}$$

where ζ is a tuning parameter. The RMS fractional fluctuation for the short-scale component is

$$\varepsilon_S = \left(\frac{a_S}{a}\right)^{\kappa} \varepsilon \tag{8}$$

(see Paper II, eq. 16). By replacing a and ϵ in eq. (3b) with a_S and ϵ_S and taking the same κ, we can calculate the PSDF for the short-scale component P_S. The PSDF for the long-scale component is calculated by $P_L(m) = P(m) - P_S(m)$. Paper I applied the Markov approximation to the long-scale component to analytically estimate the intensity time trace, and the Born approximation to the short-scale component to estimate the scattering loss as $\mathrm{e}^{-g_{S0}V_0 t}$, where g_{S0} is the total scattering coefficient for P_S. The intensity is written as

$$I_{La}(r,t) = w_L(r,t) \otimes b_L(r,t) \otimes G_g(r,t)\mathrm{e}^{-g_{S0}V_0 t} \otimes s(t), \tag{9}$$

where $G_g = \frac{1}{4\pi r^2 V_0}\delta(t - \frac{V_0 t}{r})$ is the Green function in a uniform medium, w_L and b_L are the wandering and the broadening terms derived by using the Markov approximation for P_L (see Paper II, eqs 23 and 26). We call this approximation the spectrum division

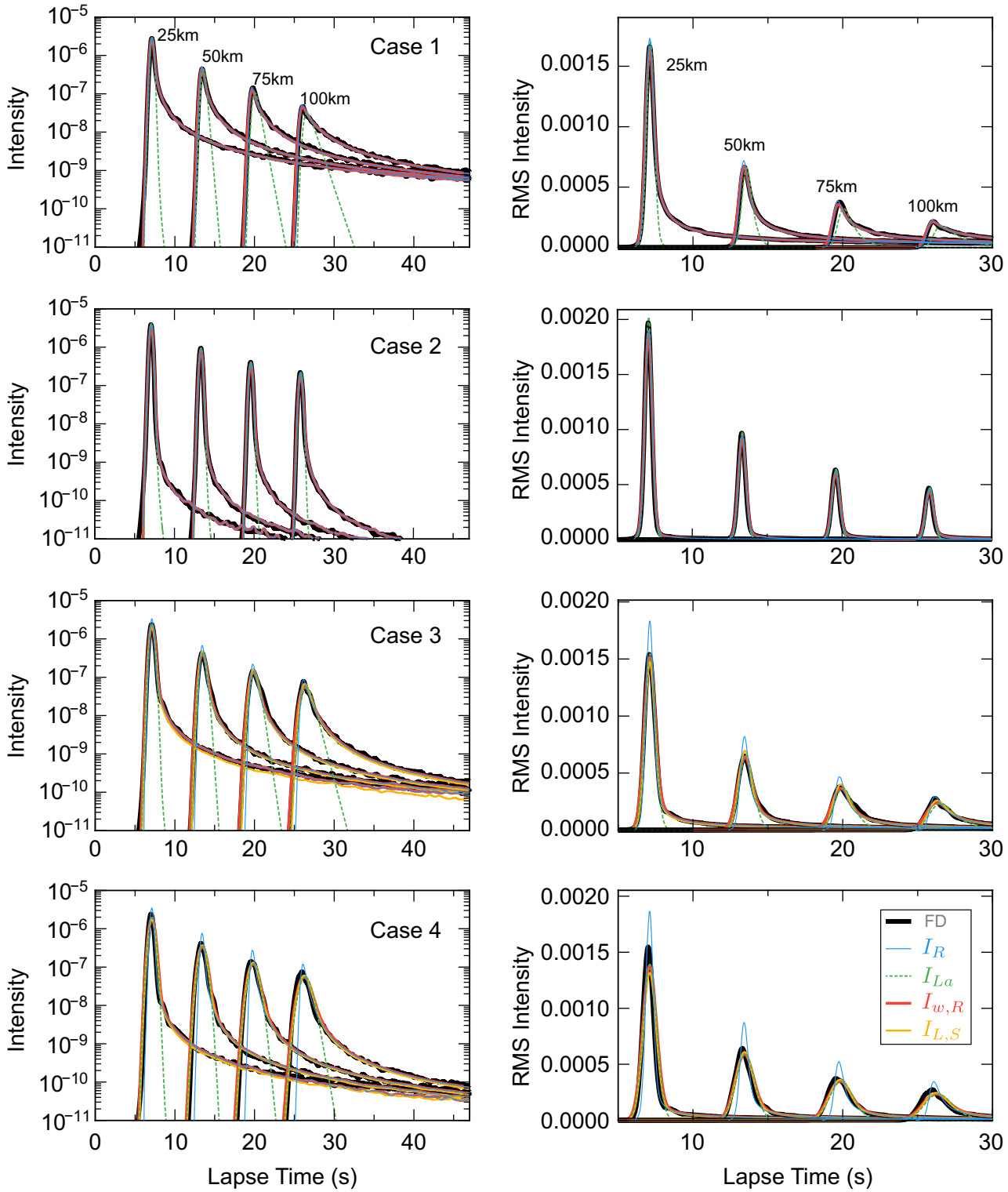

Figure 6. Comparison of intensities calculated by FD simulations with those by statistical methods for four cases at distances of 25, 50, 75 and 100 km. Figures in the left column are semi-log plots and those on the right column are linear scale plot of the square root of the intensity. Black, blue, green, red and yellow lines indicate intensities derived by FD simulations, the RTE with the Born approximation (I_{R}), the spectrum division method I (I_{La}), the RTE with the Born approximation including the wandering effect ($I_{\mathrm{w,R}}$) and the spectrum division method II ($I_{\mathrm{L,S}}$), respectively. $\zeta = 0.75$ for all cases in the spectrum division method I. $\zeta = 0.13$ and 0.10 for cases 3 and 4, respectively in the spectrum division method II.

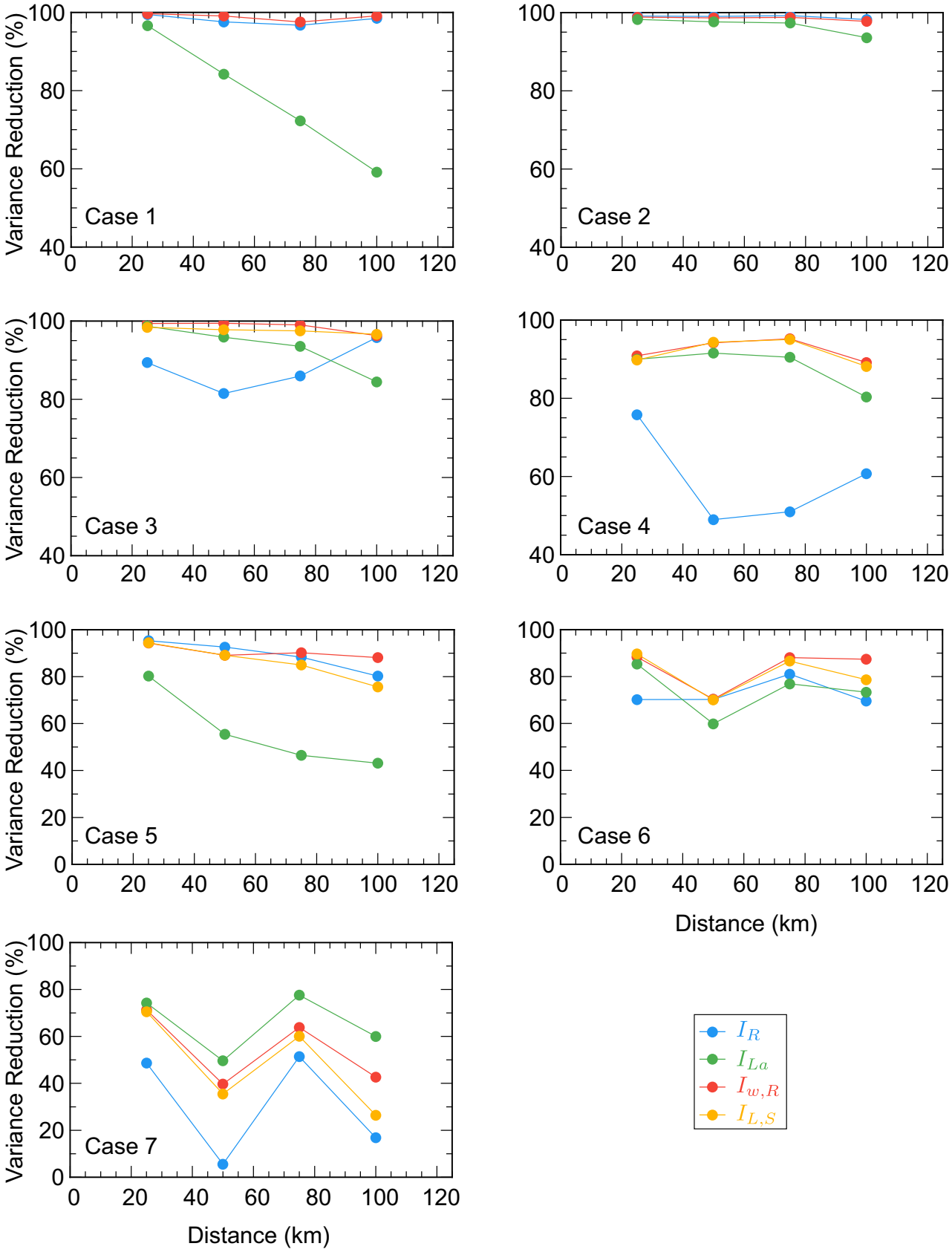

Figure 7. Variance reductions in per cent between intensities derived by theoretical methods and averaged FD intensities for all cases. Blue, green, red and yellow lines indicate intensities derived by the RTE with the Born approximation (I_R), the spectrum division method I (I_{La}), the RTE with the Born approximation including the wandering effect ($I_{w,R}$) and the spectrum division method II ($I_{L,S}$), respectively. Note that the scale of vertical axes of cases 1–4 are different from those of cases 5–7.

method I. In this case, the applicable range of the Born approximation is $\varepsilon_S^2 a_S^2 k_c^2 \ll 1$, which is a weak constraint compared to the original constraint of the Born approximation for P. For the applicability of the Markov approximation for P_L, the characteristic time (t_M) of the broadening should be much shorter than half of the traveltime,

$$t_M(k_c, \zeta, r) \ll \frac{1}{2}\frac{r}{V_0}, \tag{10}$$

where $t_M = \frac{\varepsilon^2 r^2}{2V_0 a} \ln(\zeta a k_c)$ (see Paper II, eqs 24, 25).

This method is a good approximation especially around the peak arrival since it is based on the forward scattering approximation. Sato & Fehler (2016, figs 5–7) show that syntheses of the spectrum division method I well fit those of FD simulations in 2-D random media. But, synthesized coda intensity is always underestimated since the scattering contribution of the short-scale component is introduced as the scattering loss effect only. The appropriate range of ζ for the spectrum division method I is reported as between 0.5 and 1.0 by comparing with FD simulations Sato & Fehler (2016); Tomiyama *et al.* (2017).

2.5 Spectrum division method II

Recently, Paper II proposed a method to take into account the wide-angle scattering due to the short-scale component not only for the coda intensity but also for the intensity just after the direct arrival. Using the scattering coefficient of the Born approximation to the short-scale component P_S, Paper II solved the RTE for the synthesis of the intensity Green function $G_{R,S}$. They proposed to convolve the scattering contribution of the long-scale component w_L and b_L with $G_{R,S}$ in the time domain to obtain the intensity:

$$I_{L,S}(r,t) = w_L(r,t) \otimes b_L(r,t) \otimes G_{R,S}(r,t) \otimes s(r,t), \tag{11}$$

(see Paper II, eq. 29). We call this method the spectrum division method II, which reflects well-balanced scattering contributions of long- and short-scale components. Synthesized wavelet intensities well explain those of FD simulations from the onset via the peak until early coda (see Paper II, fig. 6). In the spectrum division method II, the parameter ζ is chosen to satisfy $\varepsilon_S^2 a_S^2 k_c^2 = 0.1$.

3 RESULTS

3.1 Spatio-temporal distribution of FD intensities

We show snapshots of the spatial distribution of FD intensities at lapse times of 10, 20 and 40 s for cases 1–4 in Fig. 5. The intensity front propagates by the velocity of 4 km s^{-1}, and the peak locates a little inside of the front in each distribution. The intensity rapidly emerges at the wave front and gradually decreases towards the source. The spatial distribution of the intensity is nearly flat in the vicinity of the source and the flat region spreads with the lapse time increasing. For case 1 (Fig. 5a), the peak intensity is the smallest and the intensity level around the source is the largest in the four cases. This is because the wide-angle scattering generates the strong coda due to rich short-scale components of the velocity fluctuation (see Fig. 1b). Since we do not take into account the intrinsic absorption in the FD simulation, the volume integral of scattered-wave intensities is conserved. For case 2 (Fig. 5b), the peak intensity is the largest and the coda intensity is the smallest due to the strong forward but weak wide-angle scattering (see Fig. 1b). The intensity at a lapse time of 40 s is below the lowest bound of the plot range.

3.2 Comparison of FD simulations with various statistical methods

The averaged FD intensity at each receiver for cases 1–4 is shown in Fig. 6. Coda intensities at different distances converge to a common decay curve especially for case 1, which means the uniform distribution of coda intensity. The envelope broadening effect is stronger for cases 3 and 4 due to the strong forward scattering. We also plot intensities based on the theoretical models: the RTE with the Born approximation (I_R, blue line), I_R with the wandering term ($I_{w,R}$, red line), the spectrum division method I (I_{La}, greed dotted line) and the spectrum division method II for cases 3 and 4 ($I_{L,S}$, orange line). In the spectrum division method I, we set $\zeta = 0.75$ Sato & Fehler (2016); Tomiyama *et al.* (2017). For cases 3 and 4, we apply the spectrum division method II, because the Born approximation for the original PSDF (P) is inappropriate for the case of $\varepsilon^2 a^2 k_c^2 \gtrsim O(1)$. In the spectrum division method II, in order to satisfy the Born approximation condition $\varepsilon_S^2 a_S^2 k_c^2 = 0.1$ for P_S, we set $\zeta = 0.13$ and 0.10 for cases 3 and 4, respectively. These ζ values are smaller than that used in the spectrum division method I because coda waves are generated by wide-angle scattering in the spectrum division method II. In the spectrum division method I, the (early) coda is generated by scattering into the forward space, therefore ζ which controls the scattering contribution of P_L becomes large. To make the quantitative comparison between the FD and theoretical intensities, we calculate the variance reduction as

$$\text{Variance reduction}\,(r)\ \ [\%] = 100 \times \left(1 - \frac{\int_0^T (I_{FD}(r,t) - I_{th}(r,t))^2\,\mathrm{d}t}{\int_0^T I_{FD}^2(r,t)\mathrm{d}t}\right), \tag{12}$$

where I_{FD} is the FD intensity, I_{th} is the intensity derived by using the theoretical method and the upper limit of the integral T is set as 45 s for cases 1–4. For cases 5–7, T is set as 17, 22, 30 and 35 s at the propagation distances of 25, 50, 75 and 100 km, respectively. We show the variance reduction for all cases in Fig. 7. Intensity of the I_{La} (green dotted line in Fig. 6) well models the averaged FD intensity from the onset to the (very) early coda through the peak at each travel distance for cases 2–4. For case 1, the variance reduction between I_{La} and I_{FD} decreases with increasing propagation distance. The intensity of I_{La} is mainly produced by the Markov approximation. According to the comparison of intensities of the Markov approximation and those of the FD simulation, the condition of $ak_c >$ (5–8) is required Przybilla & Korn (2008); Emoto *et al.* (2010); however, $ak_c = 2.4$ for case 1. Note that I_{La} underestimates the coda intensities because the wide-angle scattering is neglected. Intensities of the RTE with the Born approximation $I_{w,R}$ (red line) and those of the spectrum division method II $I_{L,S}$ (orange line) can reproduce averaged FD intensities (black line) for the entire lapse time range.

We show the comparison of the averaged FD intensities with theoretical models for cases 5–7 in Fig. 8. For case 5, the wandering effect is small, because the long-scale component of the fluctuation is relatively small. We can recognize the shift of the peak arrival time between the averaged FD intensities (black line) and I_{La} (green dotted line) and their variance reduction is small for case 5 (see Fig. 7). Because of rich small-scale components, the Markov approximation may not be appropriate. For cases 6 and 7, I_{La} can well model the averaged FD intensities around the peak. $I_{w,R}$ (red line) and $I_{L,S}$ (orange line) agree well with averaged FD intensities (black line) from the onset until coda for cases 5–7. At a small propagation distance for case 7, $I_{w,R}$ and I_R underestimate the coda level

of FD intensity. This may be because of insufficient number of the particles in the Monte Carlo simulation. The variance reductions for cases 5–7 are smaller than those for cases 1–4 (see Fig. 7).

3.3 Distribution of intensities

In our FD simulation for cases 1–4, we have 360 realizations of traces at each propagation distance. We investigate the characteristics of the waveform ensemble. We show an example of the distribution of intensities at a propagation distance of 75 km for case 3 in Fig. 9. Intensities scatter over more than two orders of magnitude as shown in log-scale plots. At the time T1 just after the peak arrival (see the intensity trace Fig. 9a), the intensity histogram looks symmetric with respect to the mean value in the log-scale plot (see Fig. 9b). Conversely, at the time T2 in the coda, the intensity histogram shows a long tail to the lower side (see Fig. 9c). We divide the range between the maximum and the minimum of the intensities into 20 bins in log-scale to make a histogram. We calculate the reduced chi-square values by assuming the log-normal and exponential distributions. The probability of the log-normal distribution is written as

$$f_{\mathrm{LN}}(x)\mathrm{d}x = \frac{1}{\sqrt{2\pi}\sigma x}\mathrm{e}^{-\frac{(\ln x-\mu)^2}{2\sigma^2}}\mathrm{d}x, \tag{13a}$$

and that of the exponential distribution is written as

$$f_{\mathrm{Exp}}(x)\mathrm{d}x = \lambda \mathrm{e}^{-\lambda x}\mathrm{d}x, \tag{13b}$$

where x is the intensity. The parameters σ, μ and λ control the shape of each distribution. The reduced chi-square is defined as

$$\tilde{\chi}^2 = \frac{1}{d}\sum_{k=1}^{N}\frac{(O_k - E_k)^2}{E_k}, \tag{14}$$

where N is the number of bins, O_k is the number of samples within the kth bin obtained by the FD simulation and E_k is the expected value of the kth bin by assuming the log-normal or the exponential distributions. The variable d is the number of degrees of freedom. For the log-normal distribution $d = N - 3$, because there are three constraints, the total number of elements of the ensemble (total number of traces), the mean and the variance of the ensemble. For the exponential distribution $d = N - 2$, because there is only one control parameter λ and the mean and the variance are dependent. When there is a bin with no sample, we merge neighbouring bins. Therefore $N \leq 20$. We calculate $\tilde{\chi}^2$ in log-scale, because the exponential distribution has a sharp peak at $x = 0$, therefore the histogram cannot well resolve the distribution around $x = 0$. We show the reduced chi-square values and expected distributions at the lapse times of T1 and T2 in Figs 9(b) and (c), respectively. We calculate the parameter λ of the exponential distribution by using the mean value or the variance of intensities, separately. We adopt λ which leads to a smaller $\tilde{\chi}$. When $\tilde{\chi}^2 \leq O(1)$, the assumed distribution well explains the ensemble of the FD intensity. At the lapse time of T1, the log-normal distribution is better than the exponential one. Conversely, at the lapse time of T2, the exponential distribution well models the simulation result.

The lapse time dependence of $\tilde{\chi}^2$ is shown in Fig. 10. We apply the Hanning window smoothing for 20 times, almost equivalent to the Parzen window, to stabilize the variation of $\tilde{\chi}^2$. We also plot averaged FD intensities in Fig. 10. For all the cases, $\tilde{\chi}^2_{\mathrm{LN}} < \tilde{\chi}^2_{\mathrm{Exp}}$ at the beginning of the intensity trace. Conversely, $\tilde{\chi}^2_{\mathrm{LN}} > \tilde{\chi}^2_{\mathrm{Exp}}$ at the coda. The distribution gradually changes from the log-normal distribution to the exponential one. The timings of the shift from the log-normal distribution to the exponential one for cases 3 and 4 are later than those for cases 1 and 2. The strong forward scattering leads the log-normal distribution. At the late coda, scattered waves are random so the distribution of intensities becomes the exponential one. The timing of the shift of the distribution is much earlier than the transport mean free time shown in Table 1.

4 DISCUSSION

4.1 Attenuation of the peak intensity

In the conventional seismological attenuation measurements, the peak intensity of an individual seismogram is read irrespective of the delay time from the onset for the determination of earthquake magnitude. For example, Tsuboi (1954) proposed the decay of the maximum intensity against distance as $r^{-3.46}$ for the magnitude determination in Japan. The peak value of the intensity of each statistical model ($I_{\mathrm{w,R}}$, $I_{\mathrm{L,S}}$, I_{R} and $I_{\mathrm{L,S}}$ without the wandering term shown by solid and dashed lines) well approximates that of the averaged FD intensity (black triangle) for all the cases from 1–7 as shown in Fig. 11. However, it is not clear the relationship between the peak value of the averaged FD intensity (black triangle) and the average of individual FD intensity peak values (white triangle). When scattering is very weak as in case 2, the intensity decay curve is well described by the geometrical spreading r^{-2} since scattering loss is small. When the forward scattering is weak as in case 1, the averaged FD intensity (black triangle) well approximates the average of individual FD intensity peak values (white triangle) since the broadening effect is weak. The decay rate is a little stronger than r^{-2}. In other cases, the peak delay time of individual FD intensity (white dots) fluctuates caused by the broadening factor; therefore, the decay rate of the average of individual FD intensity peak values (white triangle) is larger than the geometrical spreading but weaker than the decay rate r^{-4} of the averaged FD intensity (black triangle), which is given by the geometrical spreading factor and the broadening factor. These simulation results can be a possible explanation of the power-law decay of the maximum intensity of a seismic wavelet with the increase of the travel distance.

4.2 Lapse time dependence of the intensity distribution

By using real observed data, Takahara & Yomogida (1992) and Nakahara & Carcole (2010) showed that the fluctuation of the coda amplitudes obeys the Rayleigh distribution. First, they estimated the averaged decay rate of the coda amplitude based on the maximum-likelihood method. Then, they analysed the fluctuation of coda amplitudes around the estimated decay rate. They analysed late coda part of the seismograms of which the time window starts from 1.5 or 2 times the traveltime of the direct *S*-wave. On the other hand, Yoshimoto *et al.* (2015) investigated the fluctuation of the peak amplitude of observed data. The observed peak amplitudes are affected not only by the random small-scale heterogeneities but also by other factors. They removed the effects of source size and the site amplification based on the coda normalization method. Also, they suppressed the effect of the radiation pattern by selecting the stations located in the large radiation pattern coefficient directions calculated by using the centroid moment tensor solution. After that, they succeeded in modelling the observed level of the fluctuation by the theoretical model and showed that the fluctuation of peak amplitude obeys the log-normal distribution. The advantage of the FD simulation is that we can continuously analyse the lapse time

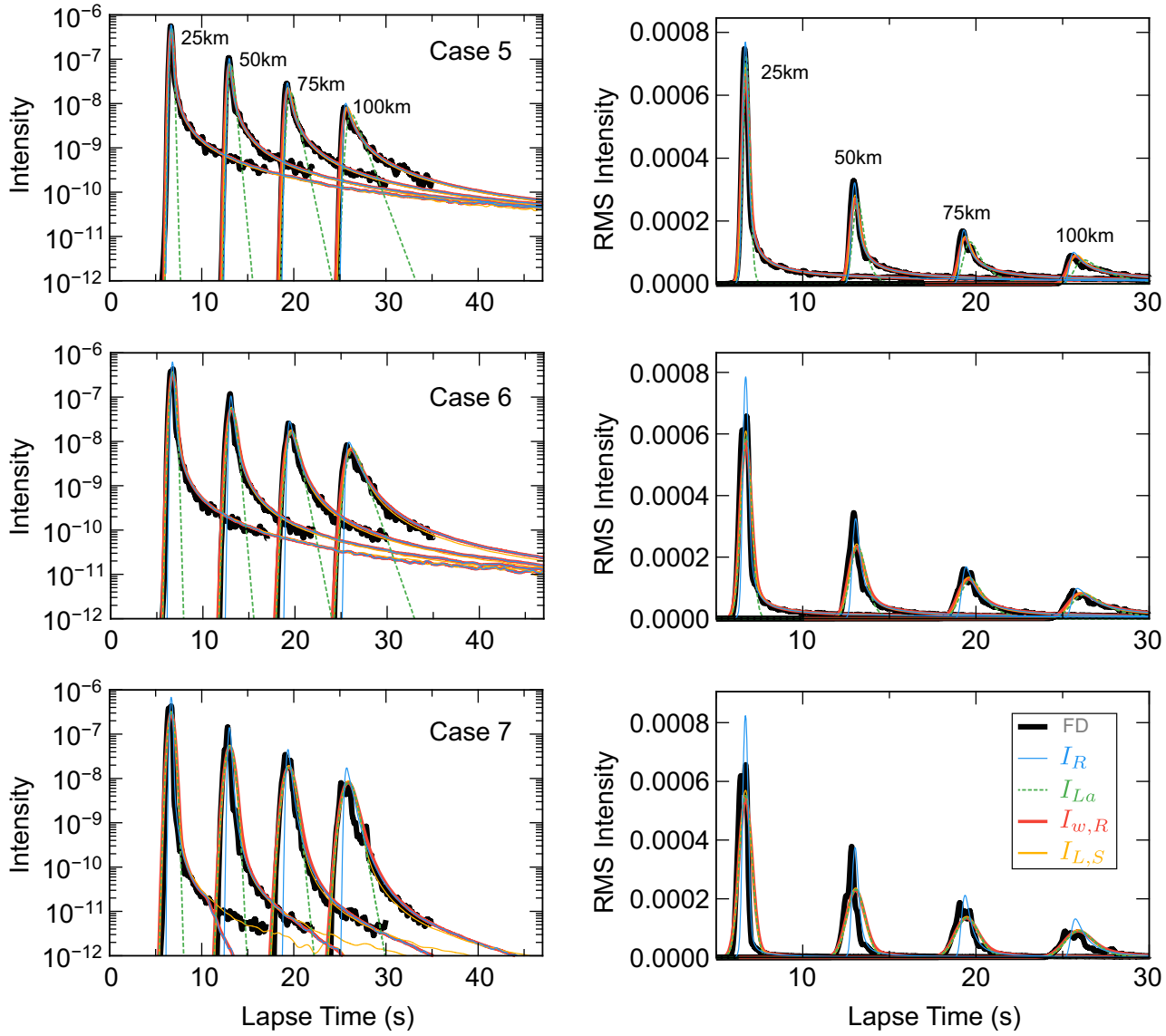

Figure 8. Same as Fig. 6 but for cases 5–7. Model setting is shown in fig. 7 of Paper II. $\zeta = 0.75$ for all cases in the spectrum division method I. $\zeta = 0.140$, 0.102 and 0.082 for cases 5, 6 and 7, respectively in the spectrum division method II.

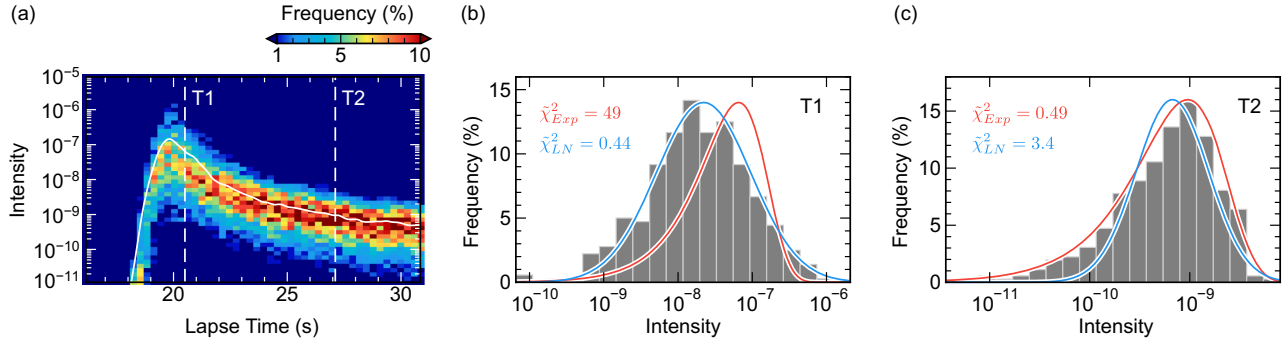

Figure 9. (a) Density plot of intensity for case 3 at a distance of 75 km. Solid white line represents the averaged FD intensity. (b) Histogram of FD intensities at the lapse time T1 indicated by a white dashed line in (a). Red and blue lines indicate the modelled exponential and log-normal distributions, respectively. We show the $\tilde{\chi}^2$ values for two distributions in the figure. (c) Same as (b) but at the lapse time T2.

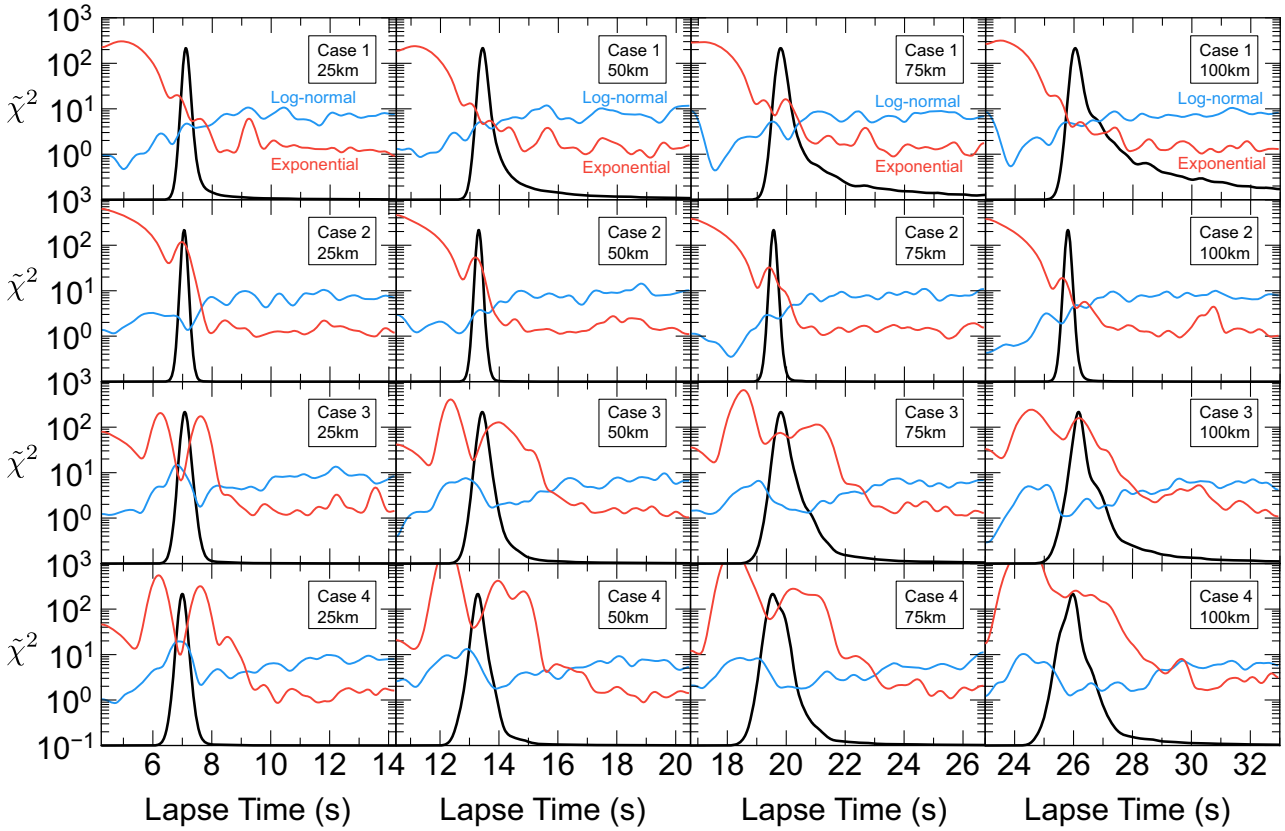

Figure 10. Lapse time dependence of $\tilde{\chi}^2$ for four cases at distances of 25, 50, 75 and 100 km. Red and blue lines indicate the $\tilde{\chi}^2$ for the exponential and the log-normal distributions, respectively. We also plot the normalized averaged FD intensity by a black solid line in linear scale.

change of the distribution of the amplitude fluctuation from the onset to the coda.

When the intensity obeys the exponential distribution, the wavefield u satisfies the normal distribution whose average is 0. This means that scattered waves have random phases and incoherent to each other. According to our result, the intensity obeys the exponential distribution in the lapse time range of coda. Conversely, when the complex phase can be written as a summation of phases along the path due to the forward scattering, the intensity obeys the log-normal distribution. Therefore, the intensity around the peak satisfies the log-normal distribution for strong forward scattering cases as 3 and 4. With the increase of the lapse time from the onset, the contribution of wide-angle scattering increases. So the distribution of intensities gradually shifts from the log-normal distribution to the exponential one. In our result, this shift is not abrupt but gradual. We need to consider other distributions to explain the gradual change of the distribution (e.g. Blanc-Benon & Juvé 1993). This theoretical consideration of the distribution will be left for future work.

5 CONCLUSION

For the study of the propagation characteristics of scaler wavelet in 3-D random media, we have synthesized the intensity, the MS amplitude, based on several stochastic methods, and then compared them with the averaged intensity calculated by FD simulations. We have examined the RTE with the Born approximation, and the spectrum division methods I and II, each of which is a balanced combination of the Markov and Born approximations. In the first four cases, random media are characterized by exponential ACFs and the target frequency is 1.5 Hz, and the average velocity is 4 km s^{-1}. The model space is a cube of 307^3 km^3 and the lapse time range is 50 s. The other three cases are the same as Paper II, where random media are characterized by von Kármán type ACFs with $\kappa = 0.1$, 0.5, and 1.0 and the target frequency is 3.0 Hz. First, we have statistically synthesized intensities in space and time domains and compared the general characteristics such as the coda excitation and the envelope broadening for the first four cases. The RTE with the Born approximation overestimates the peak intensities of the FD simulation for strong forward scattering cases. However, when the wandering term is convolved, the RTE with the Born approximation adequately models the averaged FD intensities for the entire lapse time, even in the case when the Born approximation breaks down. The spectrum division method I well models the averaged FD intensity from the onset to the early coda through its peak value except for the weak forward scattering case because of the breakdown of the parabolic approximation used in the Markov approximation. The spectrum division method II can reproduce the averaged FD intensities for the entire lapse time with enough precision even for the strong forward scattering cases: $ak_c = 24$ and $\epsilon^2 a^2 k_c{}^2 = 1.39$. The decay rate of the peak intensity is controlled by the broadening effect due to the long-scale component of the medium heterogeneity. It shifts from r^{-2} to r^{-4} with the increase of the propagation distance. This power-law decay rate is consistent with the empirical method for the magnitude determination. By investigating the distribution of intensities of FD simulation, we found that the distribution changes from the log-normal distribution near around the onset to the exponential one in the coda range. This change can be considered as the

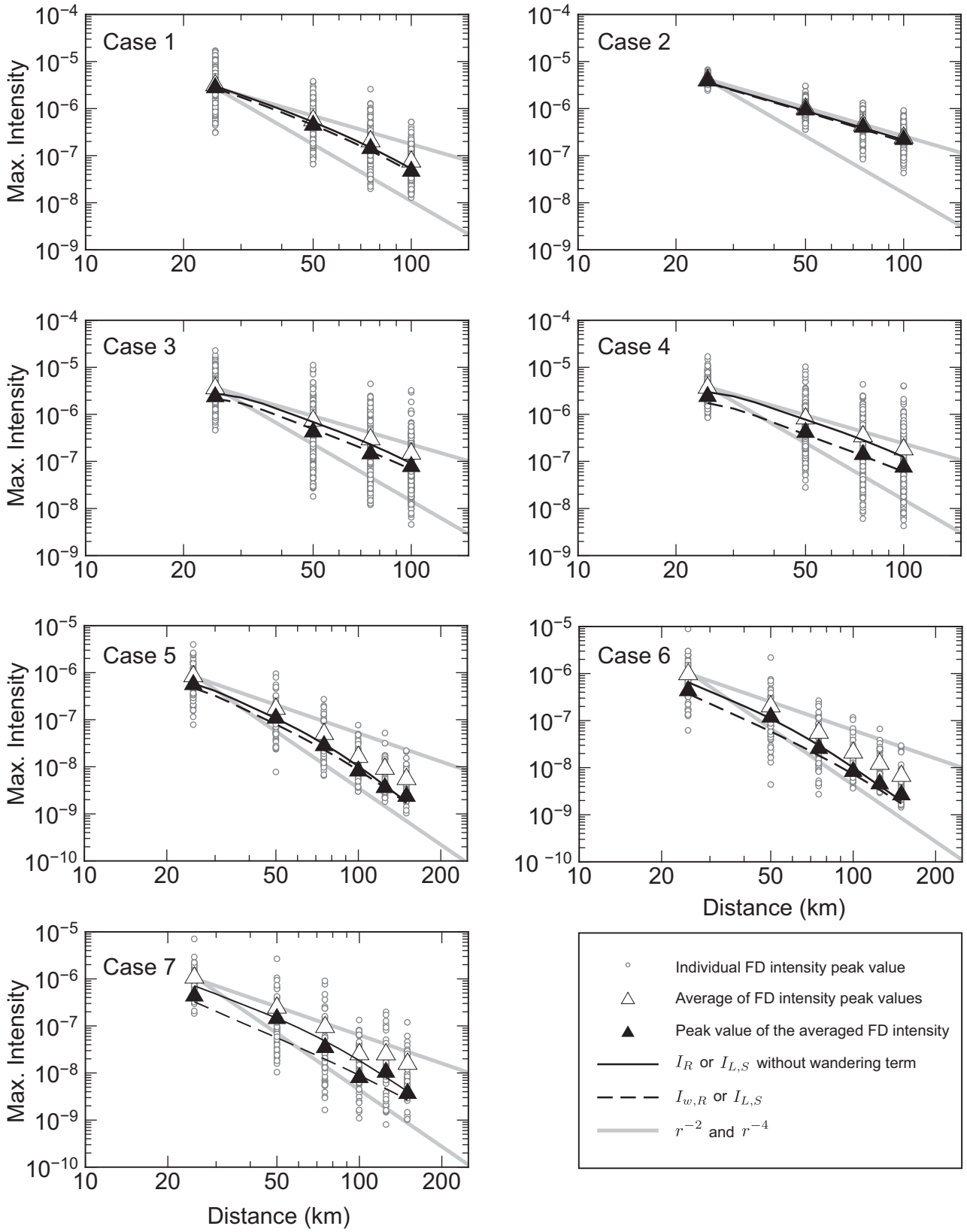

Figure 11. Attenuation of the peak value of FD intensity for cases 1–7. Circle and white triangle represent the peak values of the FD intensities and the average of them, respectively. Black triangle indicates the peak value of the averaged FD intensity. Black dashed and solid lines indicate the peak intensities of $I_{\mathrm{w,\,R}}$ (or $I_{\mathrm{L,\,S}}$) and I_{R} (or $I_{\mathrm{L,\,S}}$ without the wandering term), respectively. Two grey lines in each figure indicate the attenuation rates of r^{-2} and r^{-4}.

shift from the dominance of forward scattered waves to incoherent scattered waves with random phases in wide angles.

ACKNOWLEDGEMENTS

We would like to thank Piero Poli, an anonymous reviewer and the editor, Ana Ferreira for their helpful comments to improve this manuscript. Computations were conducted on the Earth Simulator at the JAMSTEC under the support of a joint research project between Earthquake Research Institute, the University of Tokyo, and Center of Earth Information Science and Technology entitled 'Numerical simulations of seismic- and tsunami-wave propagation in 3-D heterogeneous earth'. We have used the computer system of the Earthquake and Volcano Information Center of the Earthquake Research Institute, the University of Tokyo to create random media. We used the Hi-net data in Fig. 1, provided by National Research Institute for Earth Science and Disaster Resilience (http://www.hinet.bosai.go.jp/).

REFERENCES

Aki, K. & Chouet, B., 1975. Origin of coda waves: source, attenuation, and scattering effects, *J. geophys. Res.,* **80**(23), 3322–3342.

Blanc-Benon, ph. & Juve, D., 1993. Intensity fluctuations of spherical acoustic waves propagating through thermal turbulence, *Waves in Random Media,* **3:2,** 71–83, doi:10.1088/0959-7174/3/2/002.

Chandrasekhar, S., 1960. *Radiative Transfer,* Dover.

Chernov, L.A., 1960. *Wave Propagation in a Random Medium,* McGraw-Hill.

Emoto, K., Sato, H. & Nishimura, T., 2010. Synthesis of vector wave envelopes on the free surface of a random medium for the vertical incidence of a plane wavelet based on the Markov approximation, *J. geophys. Res.,* **115,** B08306.

Emoto, K., Sato, H. & Nishimura, T., 2012. Synthesis and applicable condition of vector wave envelopes in layered random elastic media with anisotropic autocorrelation function based on the Markov approximation, *Geophys. J. Int,* **188**(1), 325–335.

Fehler, M., Sato, H. & Huang, L., 2000. Envelope broadening of outgoing waves in 2D random media: a comparison between the Markov approximation and numerical simulations, *Bull. seism. Soc. Am.,* **90**(4), 914–928.

Frankel, A. & Clayton, R., 1986. Finite difference simulations of seismic scattering Implications for the propagation of short-period seismic waves in the crust and models of crustal heterogeneity, *J. geophys. Res.,* **91**(B6), 6465–6489.

Furumura, T. & Chen, L., 2004. Large scale parallel simulation and visualization of 3D seismic wavefield using the Earth Simulator, *Comput. Model. Eng. Sci.,* **6,** 153–168.

Gusev, A. & Abubakirov, I., 1987. Monte-Carlo simulation of record envelope of a near earthquake, *Phys. Earth planet. Inter.,* **49,** 30–36.

Hoshiba, M., 1991. Simulation of multiple-scattered coda wave excitation based on the energy conservation law, *Phys. Earth planet. Inter.,* **67**(1–2), 123–136.

Ikelle, L.T., Yung, S.K. & Daube, F., 1993. 2-D random media with ellipsoidal autocorrelation functions, *Geohysics,* **58,** 1359–1372.

Imperatori, W. & Mai, P., 2013. Broad-band near-field ground motion simulations in 3-dimensional scattering media, *Geophys. J. Int.,* **192**(2), 725–744.

Ishimaru, A., 1978. *Wave Propagation and Scattering in Random Media,* Academic Press.

Jannaud, L., Adler, P. & Jacquin, C., 1991. Spectral analysis and inversion of codas, *J. geophys. Res.,* **96,** 18 215–18 231.

Korn, M. & Sato, H., 2005. Synthesis of plane vector-wave envelopes in 2-D random elastic media based on the Markov approximation and comparison with finite difference simulations, *Geophys. J. Int,* **161**(3), 839–848.

Lee, L. & Jokipii, J., 1975. Strong scintillations in astrophysics. II. A theory of temporal broadening of pulses, *Astrophys. J.,* **201,** 532–543.

Margerin, L., 2005. Introduction to radiative transfer of seismic waves, in *Seismic Earth: Array Analysis of Broad-band Seismograms,* chap.14, pp. 229–252, ed. Nolet, L.A., AGU.

Nakahara, H. & Carcole, E., 2010. Maximum-likelihood method for estimating coda Q and the Nakagami-m parameter, *Bull. seism. Soc. Am.,* **100,** 3174–3182.

Obara, K., Kasahara, K., Hori, S. & Okada, Y., 2005. A densely distributed high-sensitivity seismograph network in Japan: Hi-net by National Research Institute for Earth Science and Disaster Prevention, *Rev. Sci. Instrum,* **76,** 021301, doi:10.1063/1.1854197.

Obermann, A., Planès, T., Céline, H. & Campillo, M., 2016. Lapse-time-dependent coda-wave depth sensitivity to local velocity perturbations in 3-D heterogeneous elastic media, *Geophys. J. Int.,* **207**(1), 59–66.

Okada, Y., Kasahara, K., Hori, S., Obara, K., Sekiguchi, S., Fujiwara, H. & Yamamoto, A., 2004. Recent progress of seismic observation network in Japan –H-net, F-net, K-NET and KiK-net, *Earth Planets Space,* **56,** xv–xviii, doi:10.1186/BF03353076.

Przybilla, J. & Korn, M., 2008. Monte Carlo simulation of radiative energy transfer in continuous elastic random media-three-component envelopes and numerical validation, *Geophys. J. Int.,* **173**(2), 566–576.

Przybilla, J., Wegler, U. & Korn, M., 2009. Estimation of crustal scattering parameters with elastic radiative transfer theory, *Geophys. J. Int.,* **178**(2), 1105–1111.

Rytov, S., Kravcov, J. & Tatarskii, V., 1989. *Principles of Statistical Radiophysics 4: Wave Propagation Through Random Media,* Springer-Verlag.

Saito, T., Sato, H., Fehler, M. & Ohtake, M., 2003. Simulating the envelope of scalar waves in 2D random media having power-law spectra of velocity fluctuation, *Bull. seism. Soc. Am.,* **93**(1), 240–252.

Sato, H., 1989. Broadening of seismogram envelopes in the randomly inhomogeneous lithosphere based on the parabolic approximation: Southeastern Honshu, Japan, *J. geophys. Res.,* **94**(B12), 17 735–17 747.

Sato, H., 2006. Synthesis of vector wave envelopes in three-dimensional random elastic media characterized by a Gaussian autocorrelation function based on the Markov approximation: plane wave case, *J. geophys. Res,* **111**(B6), B06306.

Sato, H., 2016. Envelope broadening and scattering attenuation of a scalar wavelet in random media having power-law spectra, *Geophys. J. Int.,* **204,** 386–398.

Sato, H. & Emoto, K., 2017. Synthesis of a scalar wavelet intensity propagating through von Kármán-type random media: joint use of the radiative transfer equation with the Born approximation and the Markov approximation, *Geophys. J. Int.,* **211,** 512–527.

Sato, H. & Fehler, M., 2016. Synthesis of wavelet envelope in 2-D random media having power-law spectra: comparison with FD simulations, *Geophys. J. Int.,* **207,** 333–342.

Sato, H., Fehler, M. & Maeda, T., 2012. *Seismic Wave Propagation and Scattering in the Heterogeneous Earth,* 2nd edn, Springer.

Sens-Schönfelder, C., Margerin, L. & Campillo, M., 2009. Laterally heterogeneous scattering explains Lg blockage in the Pyrenees, *J. geophys. Res.,* **114,** B07309.

Shapiro, S. & Keib, G., 1993. Seismic attenuation by scattering: theory and numerical results, *Geophys. J. Int.,* **114,** 373–391.

Shishov, V., 1974. Effect of refraction on scintillation characteristics and average pulse shape of pulsars, *Sov. Astron.,* **17,** 598–602.

Silva, J., Poliannikov, O.V., Fehler, M. & Turpening, R., 2018. Modeling scattering and intrinsic attenuation of crosswell seismic data in the Michigan Basin, *Geophysics,* **83**(3), WC15–WC27.

Takahara, M. & Yomogida, K., 1992. Estimation of coda Q using the maximum likelihood method, *Pure appl. Geophys.,* **139,** 255–268.

Takahashi, D., 2010. An implementation of parallel 3-D FFT with 2-D decomposition on a massively parallel cluster of multi-core processors, in *Parallel Processing and Applied Mathematics: 8th International Conference, PPAM 2009, Wroclaw, Poland, September 13-16, 2009. Revised Selected Papers, Part I,* pp. 606–614, eds Wyrzykowski, R., Dongarra, J., Karczewski, K. & Wasniewski, J., Springer, Berlin.

Tomiyama, Y., Kawahara, J. & Emoto, K., 2017. Envelopes of scalar plane wavelets propagating through 2-D random media with power-law spectra, in *IAG-IASPEI Joint Assembly,* Kobe, Japan, S03–1-01.

Tsuboi, C., 1954. Determination of the Gutenberg-Richter's Magnitude of Earthquakes occurring in and near Japan (in Japanese), *Zisin 2,* **7**(3), 185–193.

Yoshimoto, K., 2000. Monte Carlo simulation of seismogram envelopes in scattering media, *J. geophys. Res.,* **105,** 6153–6161.

Yoshimoto, K., Takemura, S. & Kobayashi, M., 2015. Application of scattering theory to *P*-wave amplitude fluctuations in the crust, *Earth Planets Space,* **67,** 199, doi:10.1186/s40623-015-0366-0.

SUPPORTING INFORMATION

Supplementary data are available at *GJI* online.

Figure S1. Example of the mergence of two random fluctuations in the x-direction, ξ_1 and ξ_2. The upper figure shows the weighting function w_1 (red) and w_2 (green) of ξ_1 and ξ_2, respectively. The lower figure shows the original ξ_1 (red), ξ_2 (green) and merged fluctuation (grey). The random fluctuation is characterized by the 2-D exponential type ACF with $a = 5$ km and $\epsilon = 0.05$.

Figure S2. Comparison of the (a) single large, (b) repeated and (c) merged random media. Single large random medium is calculated by using the 2-D FFT with the size of 4096×8192. After the FFT, we cut the medium into the size of 2822×5519 to compare the merged random medium in the same size. The repeated random medium is created by repeating a small random medium calculated by using the 2-D FFT with the size of 1024×1024 by 3×6 times. The merged random medium is created by merged 3×6 small random media whose size is 1024×1024. In the merged random medium, all small random media have different random seeds. Red squares in (b) and (c) indicate the size of the small random medium.

Figure S3. Comparison of 1-D PSDFs (a–c) and 1-D ACFs (d–f) of the single large random medium (a and d), repeated random medium (b and e) and merged random medium (c and f). The ACF is calculated along the y-direction at every grid point on the x-direction and the PSDF is the FFT of the ACF. Red and green lines indicate the averaged and theoretical ACF and PSDF, respectively. Black lines are the ACFs and PSDFs at different x positions.

Figure S4. Example of traces for cases 1 (a) and 4 (b) at a distance of 75 km. We randomly selected 10 traces from the ensemble. The vertical black line in (a) and (b) indicates the average traveltime. (c) Density plot of intensity for case 1 at a distance of 75 km. Solid white line represents the averaged FD intensity. Colour indicates the frequency of intensities. (d) Same as (c) but for case 4.

Figure S5. Required number of realizations whose average becomes $\pm 10\%$ of the ensemble average for cases 1 to 4. We plot the average value of the number of 100 trials by randomly sampling the realization.

Please note: Oxford University Press is not responsible for the content or functionality of any supporting materials supplied by the authors. Any queries (other than missing material) should be directed to the corresponding author for the paper.